An implicit nodal integration based PFEM for soil flow problems

Xue Zhang[1], Jingjing Meng[2, 3*], Shengyang Yuan[3]

1. Department of Civil Engineering and Industrial Design, University of Liverpool, Liverpool, United Kingdom

2. Department of Civil, Environmental and Natural Resources Engineering, Luleå University of Technology, Luleå, Sweden

3. MOE Key Laboratory of High-speed Railway Engineering, Southwest Jiaotong University, China

Abstract

An implicit Nodal integration based Particle Finite Element Method (N-PFEM) is developed to model soil flow problems. The governing equations are discretised by an implicit time integration scheme, while the spatial integration is conducted over cells, rather than finite elements, using a nodal integration scheme. Compared with the conventional PFEM, the developed N-PFEM requires no variable information transferring from old to new integration points when modelling large deformation problems. Additionally, the nature of implicit time integration makes the method particularly suitable for handling soil dynamic problems of low to medium frequency which are most likely scenarios in geotechnical engineering. The verification of the proposed method is achieved by reproducing two lab testings.

Keywords: PFEM, Soil flow, Large deformation, Nodal integration

----

1. Introduction

Extensive attempts have been made to tackle soil flow problems in the past decades because the large soil deformation cannot be resolved by the traditional Lagrangian Finite Element Method (FEM). Typical numerical approaches developed for this purpose can be categorized into discrete methods, such as the Discrete Element Method (DEM) (Cundall and Strack 1979) which treats soils as an assembly of rigid grains, and continuum approaches. The DEM has been implemented in both explicit (Cundall and Strack 1979, Ciantia, Arroyo et al. 2015) and implicit (Zhou, Chu et al. 2016, Meng, Cao et al. 2019) manners and succeeded not only in handling large soil deformations (Huang, da Silva et al. 2013, Lu, Tang et al. 2014, Meng, Huang et al. 2017, Kermani and Qiu 2020) but also in micromechanical investigations of geomaterials (Ciantia, Arroyo et al. 2015, Zhou, Chu et al. 2016, Jiang, Zhang et al. 2019, Zhu and Zhao 2021), despite its drawback in heavy computational demands and parameter calibrations. Continuum approaches developed include, but are not limited to, the pure mesh-based method (e.g. the FEM with remeshing techniques (Tian, Cassidy et al. 2014), the Arbitrary Lagrangian Eulerian Method (Nazem, Sheng et al. 2008, Tolooiyan and Gavin 2011), and the Coupled Eulerian Lagrangian Method (Qiu, Henke et al. 2011, Dey, Hawlader et al. 2015)), the pure particle approaches (e.g. the Smoothed Particle Hydrodynamics (Bui, Fukagawa et al. 2011, Kermani and Qiu 2020, Trujillo-Vela, Galindo-Torres et al. 2020, Yang, Bui et al. 2020)) and the hybrid methods (e.g. the Material Point Method (Soga, Alonso et al. 2016, Wang, Vardon et al. 2018, Tran and Sołowski 2019) and the Particle Finite Element Method (Zhang, Krabbenhoft et al. 2013, Dávalos, Cante et al. 2015, Monforte, Arroyo et al. 2017, Zhang, Oñate et al. 2019)).

As a hybrid method, the Particle Finite Element Method (PFEM) (Oñate, Celigueta et al. 2011, Cremonesi, Franci et al. 2020) uses particles to represent configurations but solve the governing equations by the FEM. Thus it inherits the advantages of particle approaches for handling large deformation and the solid mathematical foundations of the FEM. Originated in fluid mechanics for fluid-structure interactions (Oñate, Idelsohn et al. 2004), the PFEM has been extended for geotechnical problems such as granular flows (Cante, Dávalos et al. 2014, Zhang, Krabbenhoft et al. 2014, Dávalos, Cante et al. 2015, Zhang, Ding et al. 2016, Jin, Yuan et al. 2020), soil-structure interaction problems (Oñate, Celigueta et al. 2011, Zhang, Krabbenhoft et al. 2013, Zhang, Sheng et al. 2015, Monforte, Arroyo et al. 2017, Monforte, Arroyo et al. 2018, Sabetamal, Carter et al. 2021), consolidation problems (Yuan, Zhang et al. 2019), subaerial and submarine landslides (Zhang, Krabbenhoft et al. 2014, Salazar, Irazábal et al. 2016, Cremonesi, Ferri et al. 2017, Zhang, Oñate et al. 2019, Zhang, Wang et al. 2019, Mulligan, Franci et al. 2020, Yuan, Liu et al. 2020, Jin, Yin et al. 2021), debris flows (Franci and Zhang 2018), etc. Despite its advantages in modelling large deformation problems, a drawback of the conventional PFEM for modelling geotechnical problems is the requirement of variable mapping from old to new integration points after mesh generation (Zhang, Krabbenhoft et al. 2013, Monforte, Arroyo et al. 2017). This operation is essential in the conventional PFEM when handling soils which are history-dependent materials. The presence of low-quality meshes regardless of the re-construction of meshes based on particles is another drawback of the PFEM. This is because large deformations disturb the spatial distribution of particles that meshes constructed based on these particles may have small angles and edges.

In this paper, an implicit Nodal integration based PFEM (N-PFEM) is developed to simulate geotechnical problems with soil flows. The developed N-PFEM is an extension of the PFEM in (Zhang, Krabbenhoft et al. 2013, Zhang, Oñate et al. 2019) with difference in the integral over cells rather than elements. The nodal integration enables the use of three-node triangular elements without volumetric locking issue and eliminates the requirement of variable mapping from integration points. Due to the implicit nature, the developed N-PFEM is more suitable to simulate geotechnical problems in quasi-static processes (e.g. cone penetration tests and foundation consolidations) or of dynamics with low to medium frequency (e.g. soil responses in earthquake-induced landslides and rainfall-induced debris flow) that are the most likely scenarios in practice. Last but not least, as the FE formulation in the N-PFEM is developed using the generalized Helinger-Reissner (HR) variational principle, the solutions are resolved with second-order cone programming (Zhang, Oñate et al. 2019). It possesses numerous advantages such as the convergence properties, straightforward treatment of contacts and singularities in yield criterion, etc., as indicated in (Zhang, Krabbenhoft et al. 2013, Zhang, Oñate et al. 2019). To show its correctness and robustness, the proposed N-PFEM is adopted to simulate problems in both quasi-static and dynamic processes.

2. Nodal integration based Particle Finite Element Method (N-PFEM)

2.1 Min-max problem

A Nodal integration based finite element method in Second Order Cone Programming (SOCP) is first developed in this section. According to (Zhang, Oñate et al. 2019), the time discretised governing equations for dynamic analysis of elastoplastic models with volume Ω and boundary Γ are equivalent to the following min-max problem

$$
\begin{aligned}
\min_{\Delta \mathbf{u}} \max_{(\boldsymbol{\sigma},\mathbf{r})_{n+1}} \quad & \int_\Omega \boldsymbol{\sigma}_{n+1}^T \nabla^T(\Delta\mathbf{u})\mathrm{d}\Omega + \int_\Omega \frac{1-\theta_1}{\theta_1}\boldsymbol{\sigma}_n^T \nabla^T(\Delta\mathbf{u})\mathrm{d}\Omega - \int_\Omega \tilde{\mathbf{b}}^T \Delta\mathbf{u}\mathrm{d}\Omega - \int_{\Gamma_t} \tilde{\mathbf{t}}^T \Delta\mathbf{u}\mathrm{d}\Gamma \\
& -\frac{1}{2}\int_\Omega \Delta\boldsymbol{\sigma}^T C \Delta\boldsymbol{\sigma}\mathrm{d}\Omega - \frac{1}{2}\int_\Omega \mathbf{r}_{n+1}^T \frac{\Delta t^2}{\tilde{\rho}}\mathbf{r}_{n+1}\mathrm{d}\Omega + \int_\Omega \mathbf{r}_{n+1}^T \Delta\mathbf{u}\mathrm{d}\Omega \\
\text{subject to} \quad & F(\boldsymbol{\sigma}_{n+1}) \le 0
\end{aligned}
\tag{1}
$$

where $\Delta\mathbf{u}$ is the displacement increment, $\boldsymbol{\sigma}$ is the stress, $\mathbf{r}$ is the dynamic force, C is the elastic compliance matrix, F is the yield function, $\tilde{\mathbf{b}} = \frac{1}{\theta_1}\mathbf{b} + \tilde{\rho}\frac{\mathbf{v}_{\mathrm{n}}}{\Delta t}$ and $\tilde{\mathbf{t}} = \frac{1}{\theta_1}\bar{\mathbf{t}}$ are known variables where $\mathbf{b}$ is the unit weight, $\mathbf{v}_{\mathrm{n}}$ is the velocity at t_n, $\bar{\mathbf{t}}$ is the prescribed traction on the boundary and $\tilde{\rho} = \frac{\rho}{\theta_1\theta_2}$ with ρ being the density. Subscripts n+1 and n refer to the corresponding states at t_{n+1} and t_n. θ_1 and θ_2 are the time integration parameters for the standard θ-method, taking values in [0, 1] and ∇ is the linear strain-displacement differential operator. The time integration scheme is unconditionally stable provided that $\theta_1 \geq \frac{1}{2}$ and $\theta_2 \geq \frac{1}{2}$ (Zhang, Krabbenhoft et al. 2013) while it coincides with the backward Euler scheme if $\theta_1 = \theta_1 = 1$ (Wang, Zhang et al. 2021).

For Mohr-Coulomb model, the yield criterion is

$$F = \sqrt{(\sigma_{xx} - \sigma_{yy})^2 + 4\sigma_{xy}^2} + (\sigma_{xx} + \sigma_{yy})\sin\phi - 2c\cos\phi \tag{2}$$

where ϕ is the friction angle and c is the cohesion. When plastic flow is non-associated with a dilation angle of ψ, the yield criterion is then approximated by

$$F \approx F^* = \sqrt{(\sigma_{xx} - \sigma_{yy})^2 + 4\sigma_{xy}^2} + (\sigma_{xx} + \sigma_{yy})\sin\psi - 2\tilde{c}\cos\psi \tag{3}$$

according to (Zhang, Sheng et al. 2016) where $\tilde{c}$ is

$$\tilde{c} = c\frac{\cos\phi}{\cos\psi} + \frac{1}{2}\left(\tan\psi - \frac{\sin\phi}{\cos\psi}\right)\left(\sigma_{xx} + \sigma_{yy}\right)_0 \tag{4}$$

with subscript 0 referring to the current, known state which means $\tilde{c}$ is a known constant updated at the end of each time step.

2.2 Spatial discretisation

The min-max problem (1) is then discretised in space using three node triangular elements and node-based cells, for instance Ω_k^s, are constructed by connecting the centroid of each triangle to the corresponding three mid-edge points (Figure 1).

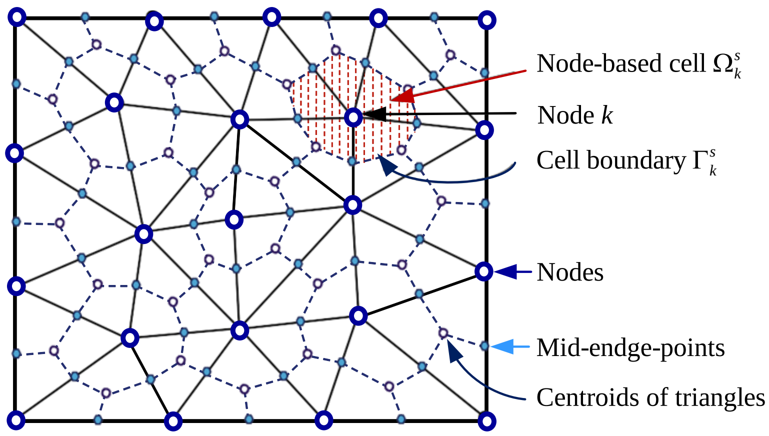

Figure 1 Node-based cells (also called smoothing domains) based on triangle mesh (after (Meng, Zhang et al. 2020)).

The displacement $\mathbf{u}$ and dynamic force $\boldsymbol{r}$ are approximated over the three node triangular element

$$\mathbf{u} \approx \mathbf{N}_{\mathrm{u}} \hat{\mathbf{u}} \tag{5}$$

$$\boldsymbol{r} \approx \mathbf{N}_{\mathrm{r}} \hat{\boldsymbol{r}} \tag{6}$$

where $\hat{\mathbf{u}}$ and $\hat{\boldsymbol{r}}$ are vectors consisting of displacements and dynamic forces at mesh nodes, and $\mathbf{N}_{\mathrm{u}}$ and $\mathbf{N}_{\mathrm{r}}$ are matrices of shape functions. The strain over finite element is

$$\boldsymbol{\varepsilon} \approx \nabla(\mathbf{N}_{\mathrm{u}}\hat{\mathbf{u}}) = \mathbf{B}_{\mathrm{u}}\hat{\mathbf{u}} \quad \text{with} \quad \mathbf{B}_{\mathrm{u}} = \nabla\mathbf{N}_{\mathrm{u}} \tag{7}$$

For each cell, we assume both the stress and strain are uniform. The strain at each cell is then estimated as a weighted average of the strain at all the one-third elements adjacent to the node

$$\bar{\boldsymbol{\varepsilon}}_k = \frac{1}{\mathrm{A}_k^c}\sum_{i=1}^{N_s}\frac{1}{3}\mathrm{A}_i^e\boldsymbol{\varepsilon}_i^e = \bar{\mathbf{B}}_k\hat{\mathbf{u}}_i^e \quad \text{with} \quad \bar{\mathbf{B}}_k = \frac{1}{\mathrm{A}_k^s}\sum_{i=1}^{N_s}\frac{1}{3}\mathrm{A}_i^e\mathbf{B}_i^e \tag{8}$$

where i is the element number and A_i^e, $\boldsymbol{\varepsilon}_i^e$, $\mathbf{B}_i^e$ and $\hat{\mathbf{u}}_i^e$ are the area, the strain, the strain gradient matrix and the displacement of the ith triangular element, respectively; N_s is the total number of elements adjacent to the kth node; and $\mathrm{A}_k^c = \sum_{i=1}^{N_s}\frac{1}{3}\mathrm{A}_i^e$ is the area of the kth cell Ω_k^c. For simplicity, the strain over a cell is written as

$$\boldsymbol{\varepsilon} = \nabla\mathbf{u} = \bar{\mathbf{B}}\hat{\mathbf{u}} \tag{9}$$

The stress over the cell is expressed as

$$\boldsymbol{\sigma} \approx \mathbf{N}_{\sigma}\bar{\boldsymbol{\sigma}} \tag{10}$$

where $\bar{\boldsymbol{\sigma}}$ is the vector of stress components at the node of the cell; and $\mathbf{N}_{\sigma}$ is in fact an identity matrix.

Substituting Eqs. (5), (6), (9) and (10) into the min-max problem (1) leads to

$$\begin{aligned} &\min_{\Delta\hat{\mathbf{u}}}\ \max_{(\hat{\boldsymbol{\sigma}},\hat{\mathbf{r}})_{\mathrm{n+1}}} \quad \Delta\hat{\mathbf{u}}^{\mathrm{T}}\mathbf{B}^{\mathrm{T}}\bar{\boldsymbol{\sigma}}_{\mathrm{n+1}} - \frac{1}{2}\Delta\bar{\boldsymbol{\sigma}}_{\mathrm{n+1}}^{\mathrm{T}}\mathbf{C}\Delta\bar{\boldsymbol{\sigma}}_{\mathrm{n+1}} - \frac{1}{2}\Delta t^2\hat{\mathbf{r}}_{\mathrm{n+1}}^{\mathrm{T}}\mathbf{D}_{\mathrm{r}}\hat{\mathbf{r}}_{\mathrm{n+1}} + \Delta\hat{\mathbf{u}}_{\mathrm{n+1}}^{\mathrm{T}}\mathbf{A}^{\mathrm{T}}\hat{\mathbf{r}}_{\mathrm{n+1}} - \Delta\hat{\mathbf{u}}^{\mathrm{T}}\tilde{\mathbf{f}} \\ &\text{subject to} \quad F(\hat{\boldsymbol{\sigma}}_{\mathrm{n+1}}) \leq 0 \end{aligned} \tag{11}$$

where

$$
\begin{aligned}
&\underline{\mathbf{B}^{\mathrm{T}} = \int_{\Omega} (\bar{\mathbf{B}})^{\mathrm{T}} \mathbf{N}_{\sigma} \mathrm{d}\Omega}, \qquad \underline{\mathbf{C} = \int_{\Omega} \mathbf{N}_{\sigma}^{\mathrm{T}} C \mathbf{N}_{\sigma} \mathrm{d}\Omega}, \\
&\mathbf{D}_{\mathrm{r}} = \int_{\Omega} (\mathbf{N}_{\mathrm{u}})^{\mathrm{T}} \hat{\rho}^{-1} \mathbf{N}_{\mathrm{u}} \mathrm{d}\Omega, \ \mathbf{A}^{\mathrm{T}} = \int_{\Omega} (\mathbf{N}_{\mathrm{u}})^{\mathrm{T}} \mathbf{N}_{\mathrm{u}} \mathrm{d}\Omega, \\
&\tilde{\mathbf{f}} = \int_{\Omega} \mathbf{N}_{\mathrm{u}}^{\mathrm{T}} \tilde{\mathbf{b}} \mathrm{d}\Omega + \int_{\Gamma} \mathbf{N}_{\mathrm{u}}^{\mathrm{T}} \tilde{\mathbf{t}} \Gamma - \frac{1-\theta_1}{\theta_1} \mathbf{B}^{\mathrm{T}} \bar{\boldsymbol{\sigma}}_{\mathrm{n}}
\end{aligned}
\tag{12}
$$

Remarkably, the underlined terms in Eq. (12) are related to stresses and strains and integrated over cells using the nodal integration scheme whereas the rests are integrated over finite elements using the Gauss integration scheme.

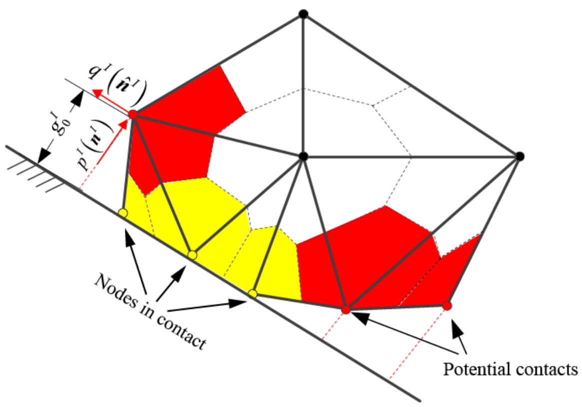

Figure 2. The boundary condition for a deformable body.

The contact between a deformable body and a rigid boundary can be handled as in the elastoplastic static cases (Meng, Zhang et al. 2020). The non-penetration conditions for a potential contact node, marked as I, are (see also Figure 2)

$$
\begin{aligned}
&g^I = g_0^I + \left(\Delta\hat{\mathbf{u}}^I\right)^{\mathrm{T}} \boldsymbol{n}^I \geq 0 \\
&p^I g^I = 0
\end{aligned}
\tag{13}
$$

where $\Delta\hat{\mathbf{u}}^I$ is the displacement increments of the node, $\boldsymbol{n}^I$ is the outward normal vector of the boundary, p^I is the contact force, g_0^I is the initial gap and g^I is the gap at the next step.

After enforcing the non-penetration conditions, the problem (11) is extended to

$$\begin{aligned}
\min_{\Delta\hat{\mathbf{u}}} \max_{(\hat{\boldsymbol{\sigma}},\hat{\mathbf{r}})_{\mathrm{n+1}},\,\boldsymbol{p},\,\boldsymbol{q}} \quad & \Delta\hat{\mathbf{u}}^{\mathrm{T}}\mathbf{B}^{\mathrm{T}}\bar{\boldsymbol{\sigma}}_{\mathrm{n+1}} - \frac{1}{2}\Delta\bar{\boldsymbol{\sigma}}_{\mathrm{n+1}}^{\mathrm{T}}\mathbf{C}\Delta\bar{\boldsymbol{\sigma}}_{\mathrm{n+1}} - \frac{1}{2}\Delta t^2\hat{\mathbf{r}}_{\mathrm{n+1}}^{\mathrm{T}}\mathbf{D}_{\mathrm{r}}\hat{\mathbf{r}}_{\mathrm{n+1}} + \Delta\hat{\mathbf{u}}_{\mathrm{n+1}}^{\mathrm{T}}\mathbf{A}^{\mathrm{T}}\hat{\mathbf{r}}_{\mathrm{n+1}} - \Delta\hat{\mathbf{u}}^{\mathrm{T}}\tilde{\mathbf{f}} \\
& -\Delta\hat{\mathbf{u}}^{\mathrm{T}}\left(\boldsymbol{n}\boldsymbol{p} + \hat{\boldsymbol{n}}\boldsymbol{q}\right) - \sum_{I=1}^{N_b} g_0^I p^I \\
\text{subject to} \quad & F(\hat{\boldsymbol{\sigma}}_{\mathrm{n+1}}) \le 0 \\
& F_b\left(\boldsymbol{p},\ \boldsymbol{q}\right) \le 0
\end{aligned} \tag{14}$$

where N_b is the total number of nodes in potential boundary contact; the normal and tangential vectors of the boundaries are collected in $\boldsymbol{n}$ and $\hat{\boldsymbol{n}}$; contact forces in the normal and tangential directions are organized into vectors $\boldsymbol{p}$ and $\boldsymbol{q}$, respectively, and $F_b\left(\boldsymbol{p},\ \boldsymbol{q}\right) \le 0$ is the cohesive-frictional contact condition as in (Meng, Zhang et al. 2020).

The minimization problem in (14) can be resolved analytically leading to the following maximization problem

$$\begin{aligned}
\max_{(\hat{\boldsymbol{\sigma}},\hat{\mathbf{r}})_{\mathrm{n+1}},\,\boldsymbol{p},\,\boldsymbol{q}} \quad & -\frac{1}{2}\Delta\bar{\boldsymbol{\sigma}}_{\mathrm{n+1}}^{\mathrm{T}}\mathbf{C}\Delta\bar{\boldsymbol{\sigma}}_{\mathrm{n+1}} - \frac{1}{2}\Delta t^2\hat{\mathbf{r}}_{\mathrm{n+1}}^{\mathrm{T}}\mathbf{D}_{\mathrm{r}}\hat{\mathbf{r}}_{\mathrm{n+1}} - \sum_{I=1}^{N_b} g_0^I p^I \\
\text{subject to} \quad & \mathbf{B}^{\mathrm{T}}\bar{\boldsymbol{\sigma}}_{\mathrm{n+1}} + \mathbf{A}^{\mathrm{T}}\hat{\mathbf{r}}_{\mathrm{n+1}} - \tilde{\mathbf{f}} - \left(\boldsymbol{n}\boldsymbol{p} + \hat{\boldsymbol{n}}\boldsymbol{q}\right) = \mathbf{0} \\
& F(\hat{\boldsymbol{\sigma}}_{\mathrm{n+1}}) \le 0 \\
& F_b\left(\boldsymbol{p},\ \boldsymbol{q}\right) \le 0
\end{aligned} \tag{15}$$

which apparently is equivalent to

$$
\begin{aligned}
\min_{\bar{\sigma}_{n+1},\, \bar{r}_{n+1},\, \boldsymbol{p},\, \boldsymbol{q}} \quad & \frac{1}{2}\Delta\bar{\boldsymbol{\sigma}}_{n+1}^{\mathrm{T}}\mathbf{C}\Delta\bar{\boldsymbol{\sigma}}_{n+1} + \frac{1}{2}\Delta t^2 \tilde{\boldsymbol{r}}_{n+1}^{\mathrm{T}}\mathbf{D}_r\tilde{\boldsymbol{r}}_{n+1} + \sum_{I=1}^{N_b} g_0^I p^I \\
\text{subject to} \quad & \mathbf{B}^{\mathrm{T}}\bar{\boldsymbol{\sigma}}_{n+1} + \mathbf{A}^{\mathrm{T}}\tilde{\boldsymbol{r}}_{n+1} = \tilde{\mathbf{f}} + \boldsymbol{n}\boldsymbol{p} + \hat{\boldsymbol{n}}\boldsymbol{q} \\
& F\left(\bar{\boldsymbol{\sigma}}_{n+1}\right) \le 0 \\
& F_b\left(\boldsymbol{p},\ \boldsymbol{q}\right) \le 0
\end{aligned}
\tag{16}
$$

Following (Zhang, Oñate et al. 2019), optimisation problem (16) can be reformulated as a standard SOCP problem

$$
\begin{aligned}
\min_{\bar{\sigma}_{n+1},\, \bar{r}_{n+1},\, \boldsymbol{p},\, \boldsymbol{q}} \quad & \dot{X} + \dot{I} + \sum_{I=1}^{N_b} g_0^I p^I \\
\text{subject to} \quad & \mathbf{B}^{\mathrm{T}}\bar{\boldsymbol{\sigma}}_{n+1} + \mathbf{A}^{\mathrm{T}}\tilde{\boldsymbol{r}}_{n+1} = \tilde{\mathbf{f}} + \boldsymbol{n}\boldsymbol{p} + \hat{\boldsymbol{n}}\boldsymbol{q} \\
& \boxed{\begin{array}{l} \boldsymbol{\xi}_{\bar{\boldsymbol{\sigma}}} = \mathbf{C}^{\frac{1}{2}}\Delta\bar{\boldsymbol{\sigma}}_{n+1},\ \dot{Y} = 1,\ (\dot{X},\ \dot{Y},\ \boldsymbol{\xi}_{\bar{\boldsymbol{\sigma}}}) \in \mathcal{K}_r \\ \mathcal{K}_r = \left\{\ (\dot{X},\ \dot{Y},\ \boldsymbol{\xi}_{\bar{\boldsymbol{\sigma}}}) \in \mathbb{R}^{m+2} \mid 2\dot{X}\dot{Y} \ge \boldsymbol{\xi}_{\bar{\boldsymbol{\sigma}}}^{\mathrm{T}}\boldsymbol{\xi}_{\bar{\boldsymbol{\sigma}}},\ \dot{X} \ge 0,\ \dot{Y} \ge 0\right\} \end{array}} \\
& \boxed{\begin{array}{l} \boldsymbol{\xi}_{\bar{\boldsymbol{r}}} = \Delta t\mathbf{D}_r^{\frac{1}{2}}\tilde{\boldsymbol{r}}_{n+1},\ \dot{J} = 1,\ (\dot{I},\ \dot{J},\ \boldsymbol{\xi}_{\bar{\boldsymbol{r}}}) \in \mathcal{K}_r \\ \mathcal{K}_r = \left\{\ (\dot{I},\ \dot{J},\ \boldsymbol{\xi}_{\bar{\boldsymbol{r}}}) \in \mathbb{R}^{m+2} \mid 2\dot{I}\dot{J} \ge \boldsymbol{\xi}_{\bar{\boldsymbol{r}}}^{\mathrm{T}}\boldsymbol{\xi}_{\bar{\boldsymbol{r}}},\ \dot{I} \ge 0,\ \dot{J} \ge 0\right\} \end{array}} \\
& F\left(\bar{\boldsymbol{\sigma}}_{n+1}\right) \le 0 \\
& F_b\left(\boldsymbol{p},\ \boldsymbol{q}\right) \le 0
\end{aligned}
\tag{17}
$$

in which the quadratic terms in the objective function are replaced by two auxiliary variables $\dot{X}$ and $\dot{I}$ with additionally constraints (e.g. the boxed terms). The minimization problem (17) can be solved using the interior-point method.

2.3 N-PFEM

Formulation (17) can be implemented in the standard PFEM framework to form N-PFEM for modelling soil flow problems. Since the terms relevant to stresses and strains (see also Eq. (12)) are integrated on cells rather than finite elements, variable mapping from old Gauss points to new Gauss points is not necessitated even handling history-dependent materials. A typical computational cycle of the N-PFEM modelling is detailed in Figure 3 for reference.

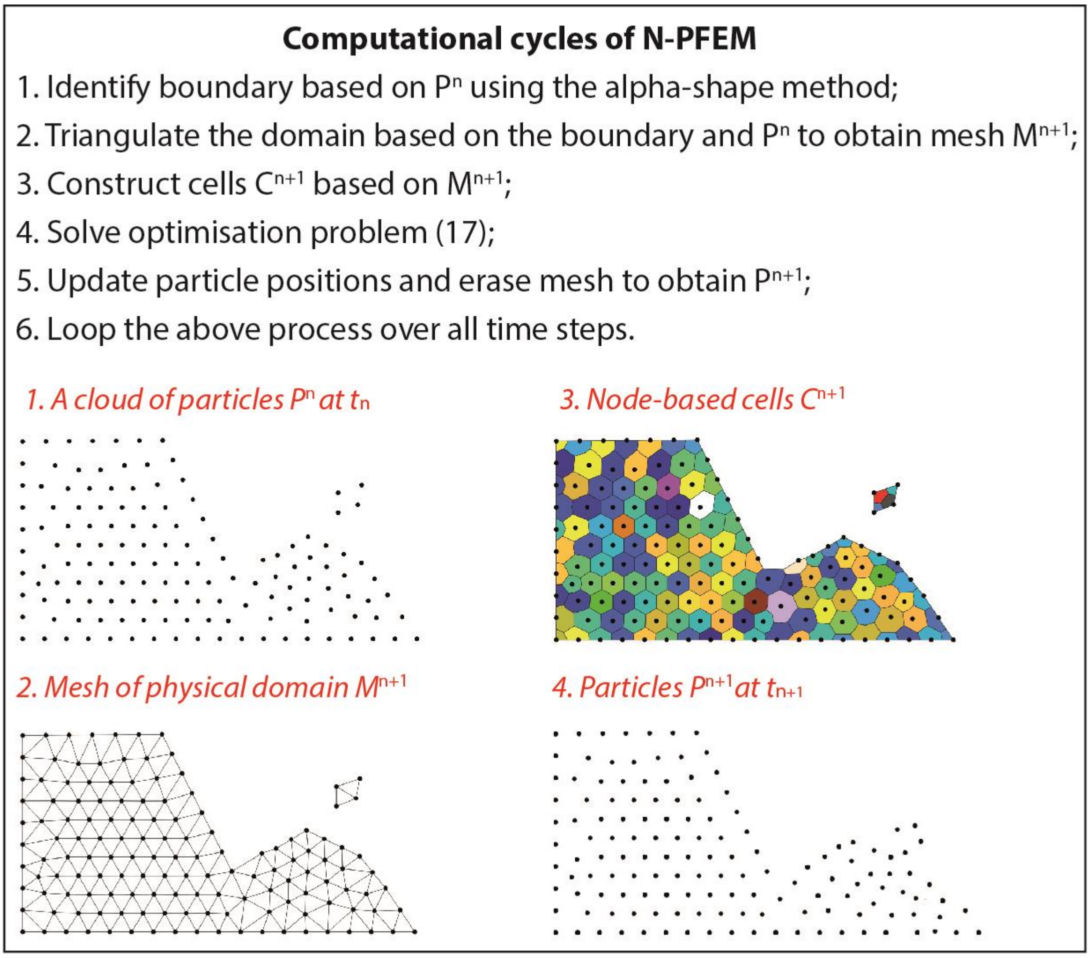

Figure 3. Computational cycles of the N-PFEM

Remarkably, the recently developed Smoothed PFEM (Zhang, Yuan et al. 2018, Yuan, Wang et al. 2019) also employs the nodal integration scheme to avoid variable mapping, its explicit nature makes the simulation very time-consuming. On the contrary, the implicit N-PFEM developed in this study is more suitable for geotechnical problems which are commonly quasi-static or low- to medium-frequency dynamic. It also enjoys some unique advantages when modelling nonlinear problems as indicated in the introduction and (Zhang, Krabbenhoft et al. 2013, Zhang, Oñate et al. 2019).

3. Numerical Examples

Two laboratory tests are reproduced using the proposed implicit N-PFEM to demonstrate its capability in modelling soil flow problems in this section.

3.1 Quasi-static granular column collapse

The N-PFEM is used to simulate the experiment of the quasi-static collapse of granular columns reported in (Mériaux 2006). The model setup is shown in *Figure 4*. Thanks to the implicit nature of the proposed method, a large time step (from 0.001 s to 0.1 s) which is adaptive to the maximum speed of granular flow are used in the simulation.

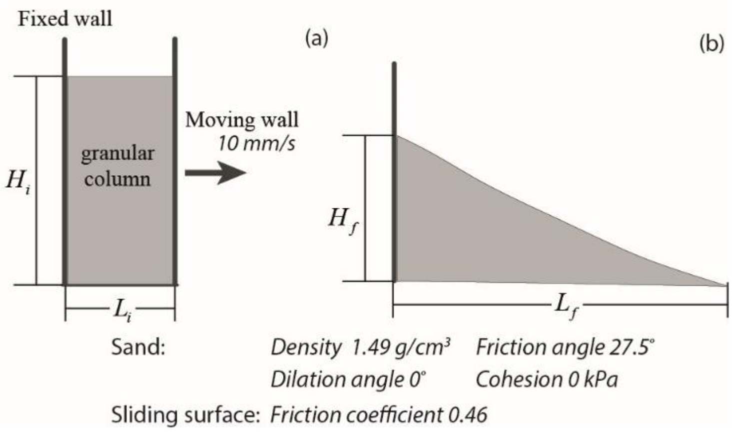

Figure 4 Schematic representation of the quasi-static fall of granular columns: (a) initial configuration and (b) final deposit

The fall of a granular column with aspect ratio A $=H_i/L_i$=5.5 is first simulated with the N-PFEM as illustrated in *Figure 5*. The heights of the left and right sides of the column in the collapse process are measured and compared with the experimental results and available DEM results (Owen, Cleary et al.

2009). As shown in *Figure 6*, a good agreement between numerical and experimental results has achieved which verifies the proposed approach for analysing granular flow.

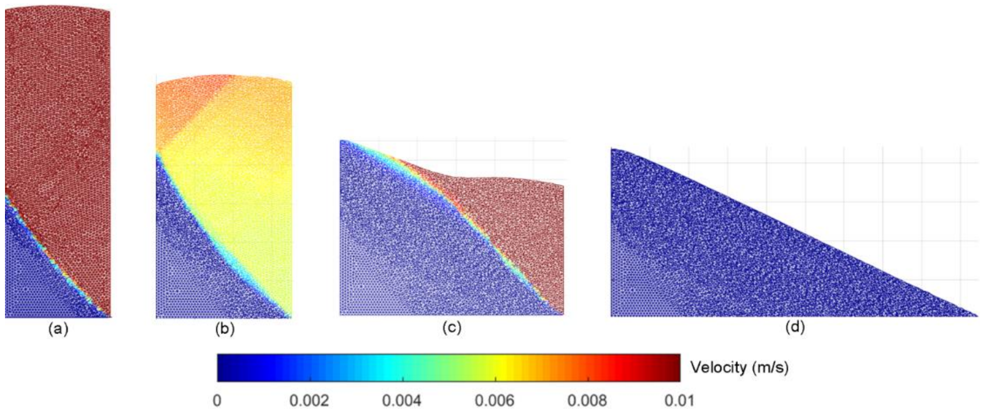

Figure 5 Evolution of granular column with time for A=5.5: (a) t/T = 0.1, (b) t/T = 0.2, (c) t/T = 0.5 and (d) t/T = 1.0, where t is simulation time and T=7.6 s is total time required in the simulation.

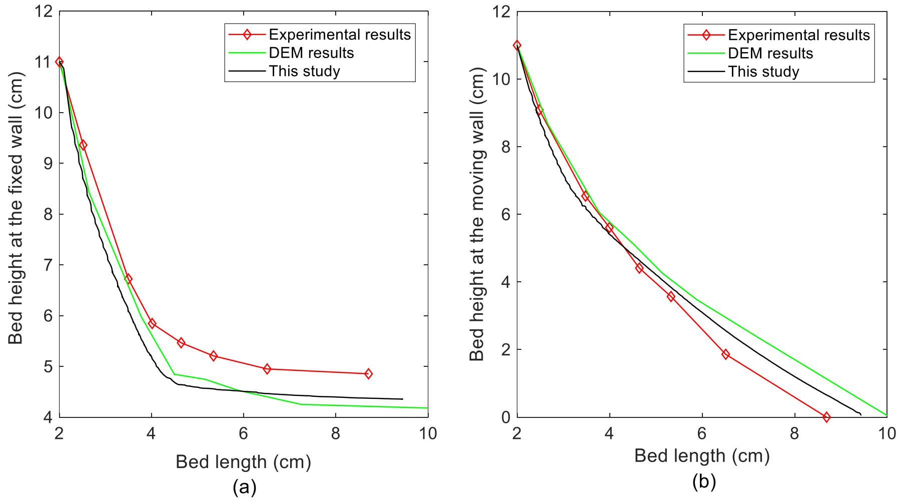

Figure 6 Evolution of bed height of the falling granular column as a function of bed length for A=5.5: (a) bed height at the fixed wall and (b) bed height at the moving wall.

Furthermore, a series of numerical tests are conducted with a varied *A* ranging from 0.1 to 7. Simulations results from the N-PFEM and the experimental data from (Mériaux 2006) are shown in *Figure 7*. Clearly, the numerical results agree well with experimental observations, both indicating power-law relationships.

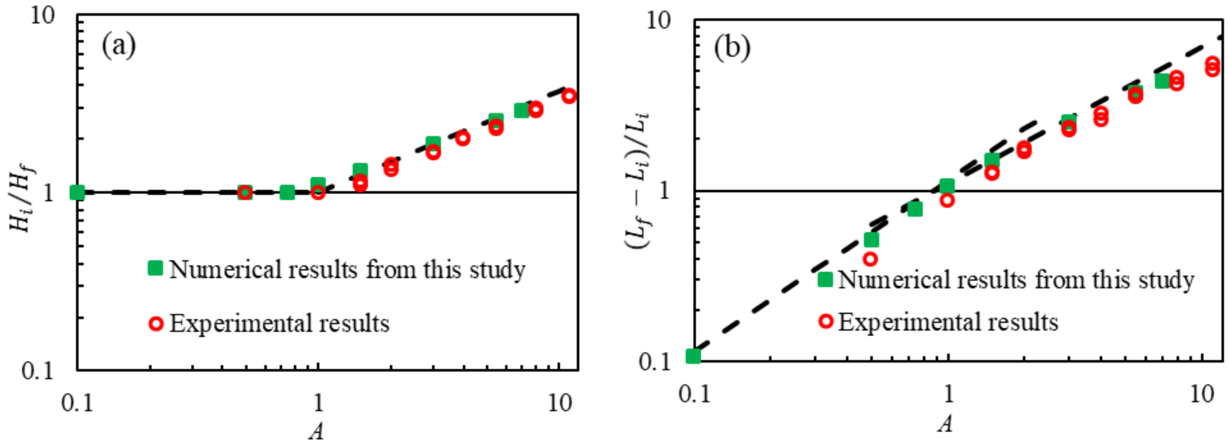

Figure 7 Deposition profile: (a) normalised final height and (b) length against the aspect ratio A.

3.2 Underwater granular flow

In this example, the multiphase flow problem is modelled with results compared with experimental and numerical results documented in (Rzadkiewicz, Mariotti et al. 1997). The setup is shown in *Figure 8*. The material parameters of the saturated sand and water are in line with these in the simulation in (Rzadkiewicz, Mariotti et al. 1997). Sliding saturated sands are of density 1985 kg/m^3 and shear strength 200 Pa. The density of water is 1000 kg/m^3 and viscous effects are neglected. The mesh size in the simulation is 0.02 m and the time step is 2×10^{-3} s.

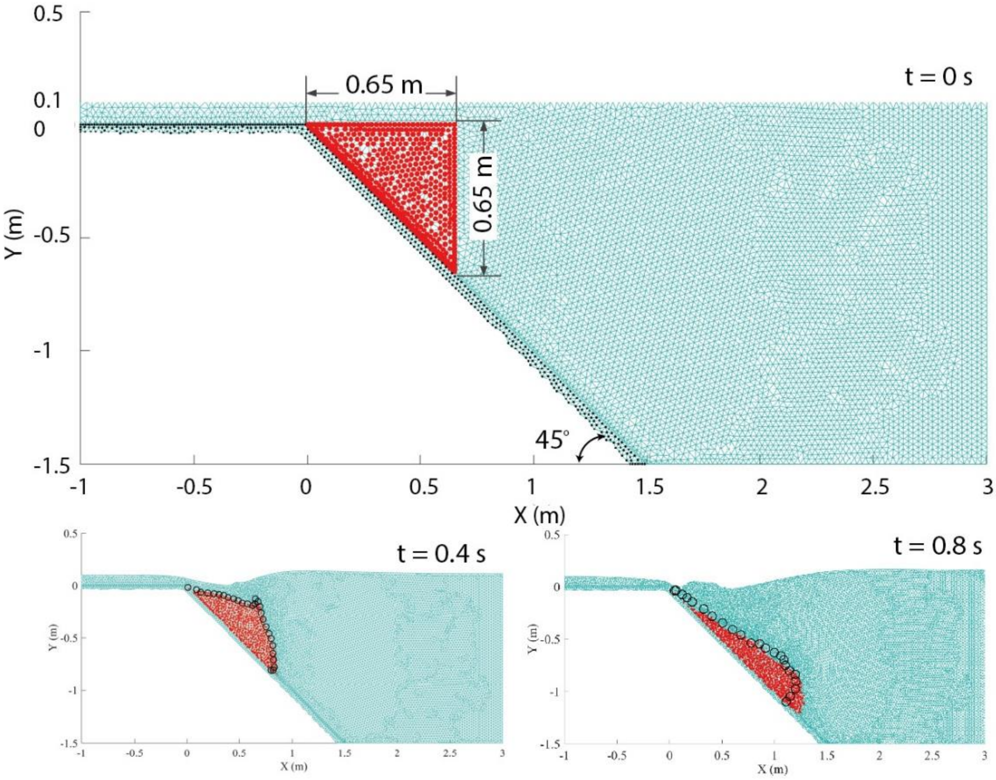

Figure 8 Evolution of underwater granular flows from N-PFEM simulations. Circles are simulation results from (Rzadkiewicz, Mariotti et al. 1997).

The snapshots of shapes of the sliding sand and the induced water surface at time instances of 0.4 s and 0.8 s are shown in *Figure 8* which agree well with these from (Rzadkiewicz, Mariotti et al. 1997). More detailed comparisons on the free water surfaces between the numerical simulations and laboratory tests are shown in *Figure 9* where a satisfactory agreement is achieved. Furthermore, our simulation was continued until reaching t=1.2 s. *Figure 10* shows that sand behaves as a fluid as it flows downwards. Sliding sand is separated into several parts surrounded by water (*Figure 10* (a)) and turbulence is observed in the sliding front (*Figure 10* (b)).

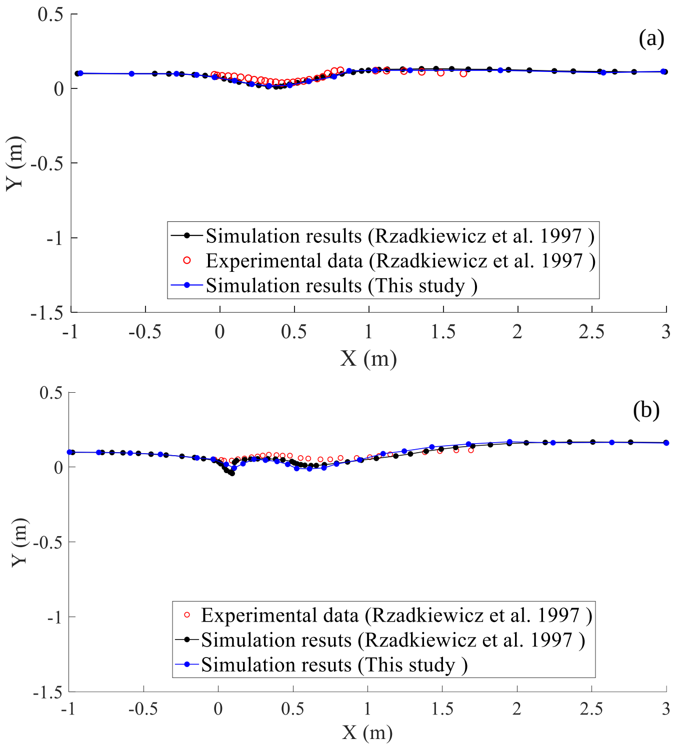

Figure 9 Water surfaces at times (a) t = 0.4 s and (b) t = 0.8 s.

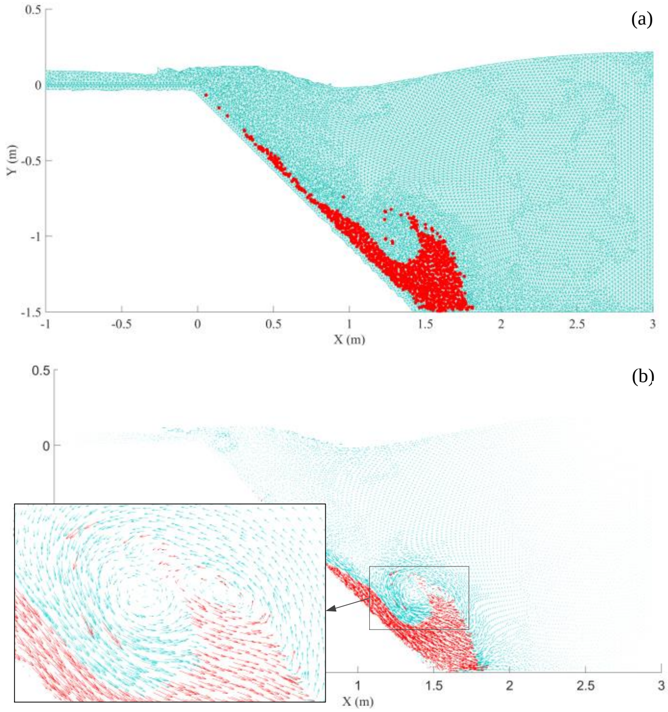

Figure 10 Simulation results at time of 1.2 s: (a) the sand mass and the induced water wave and (b) the velocity vector field.

4. Conclusions

A novel computational framework called the Nodal-integration based Particle Finite Element Method (N-PFEM) is developed for modelling soil flow problems. Compared with the conventional PFEM, the developed N-PFEM requires no variable mapping from old to new Gauss points when modelling history-dependent materials. Additionally, the implicit feature of the formulation enables the use of a large time step which is more favoured for modelling geotechnical problems which are commonly quasi-static or of low and medium frequency. Two laboratory tests (i.e., quasi-static collapse of granular columns and underwater sand flow) are considered using the proposed N-PFEM for showing its capability in handling soil flow with large deformation as well as for its verification. Good agreements between the simulation results and the reported experimental date demonstrates its correctness and robustness.

Acknowledgement

The project is supported by the New Investigator Award grant of UK Engineering and Physical Science Research Council (EP/V012169/1) and the open research fund of MOE Key Laboratory of High-speed Railway Engineering, Southwest Jiaotong University.

References

Bui, H. H., R. Fukagawa, K. Sako and J. C. Wells (2011). "Slope stability analysis and discontinuous slope failure simulation by elasto-plastic smoothed particle hydrodynamics (SPH)." Géotechnique **61**(7): 565-574.

Cante, J., C. Dávalos, J. A. Hernández, J. Oliver, P. Jonsén, G. Gustafsson and H. Å. Häggblad (2014). "PFEM-based modeling of industrial granular flows." Computational Particle Mechanics **1**(1): 47-70.

Ciantia, M. O., M. Arroyo, F. Calvetti and A. Gens (2015). "An approach to enhance efficiency of DEM modelling of soils with crushable grains." Géotechnique **65**(2): 91-110.

Cremonesi, M., F. Ferri and U. Perego (2017). "A basal slip model for Lagrangian finite element simulations of 3D landslides." International Journal for Numerical and Analytical Methods in Geomechanics **41**(1): 30-53.

Cremonesi, M., A. Franci, S. Idelsohn and E. Oñate (2020). "A state of the art review of the particle finite element method (PFEM)." Archives of Computational Methods in Engineering **27**(5): 1709-1735.

Cundall, P. A. and O. D. L. Strack (1979). "A discrete numerical model for granular assemblies." Géotechnique **29**(1): 47-65.

Dávalos, C., J. Cante, J. A. Hernández and J. Oliver (2015). "On the numerical modeling of granular material flows via the Particle Finite Element Method (PFEM)." International Journal of Solids and Structures **71**: 99-125.

Dey, R., B. Hawlader, R. Phillips and K. Soga (2015). "Large deformation finite-element modelling of progressive failure leading to spread in sensitive clay slopes." Géotechnique **65**(8): 657-668.

Franci, A. and X. Zhang (2018). "3D numerical simulation of free-surface Bingham fluids interacting with structures using the PFEM." Journal of Non-Newtonian Fluid Mechanics **259**: 1-15.

Huang, J., M. V. da Silva and K. Krabbenhoft (2013). "Three-dimensional granular contact dynamics with rolling resistance." Computers and Geotechnics **49**: 289-298.

Jiang, M., A. Zhang and T. Li (2019). "Distinct element analysis of the microstructure evolution in granular soils under cyclic loading." Granular Matter **21**(2): 39.

Jin, Y.-F., Z.-Y. Yin, X.-W. Zhou and F.-T. Liu (2021). "A stable node-based smoothed PFEM for solving geotechnical large deformation 2D problems." Computer Methods in Applied Mechanics and Engineering **387**: 114179.

Jin, Y.-F., W.-H. Yuan, Z.-Y. Yin and Y.-M. Cheng (2020). "An edge-based strain smoothing particle finite element method for large deformation problems in geotechnical engineering." International Journal for Numerical and Analytical Methods in Geomechanics **44**(7): 923-941.

Kermani, E. and T. Qiu (2020). "Simulation of quasi-static axisymmetric collapse of granular columns using smoothed particle hydrodynamics and discrete element methods." Acta Geotechnica **15**(2): 423-437.

Lu, C.-Y., C.-L. Tang, Y.-C. Chan, J.-C. Hu and C.-C. Chi (2014). "Forecasting landslide hazard by the 3D discrete element method: A case study of the unstable slope in the Lushan hot spring district, central Taiwan." Engineering Geology **183**: 14-30.

Meng, J., P. Cao, J. Huang, H. Lin, Y. Chen and R. Cao (2019). "Second-order cone programming formulation of discontinuous deformation analysis." International Journal for Numerical Methods in Engineering **118**(5): 243-257.

Meng, J., J. Huang, D. Sheng and S. W. Sloan (2017). "Granular contact dynamics with elastic bond model." Acta Geotechnica **12**(3): 479-493.

Meng, J., X. Zhang, J. Huang, H. Tang, H. Mattsson and J. Laue (2020). "A smoothed finite element method using second-order cone programming." Computers and Geotechnics **123**: 103547.

Mériaux, C. (2006). "Two dimensional fall of granular columns controlled by slow horizontal withdrawal of a retaining wall." Physics of Fluids **18**(9): 093301.

Monforte, L., M. Arroyo, J. M. Carbonell and A. Gens (2017). "Numerical simulation of undrained insertion problems in geotechnical engineering with the Particle Finite Element Method (PFEM)." Computers and Geotechnics **82**: 144-156.

Monforte, L., M. Arroyo, J. M. Carbonell and A. Gens (2018). "Coupled effective stress analysis of insertion problems in geotechnics with the Particle Finite Element Method." Computers and Geotechnics **101**: 114-129.

Mulligan, R. P., A. Franci, M. A. Celigueta and W. A. Take (2020). "Simulations of Landslide Wave Generation and Propagation Using the Particle Finite Element Method." Journal of Geophysical Research: Oceans **125**(6): e2019JC015873.

Nazem, M., D. Sheng, J. P. Carter and S. W. Sloan (2008). "Arbitrary Lagrangian‐Eulerian method for large‐strain consolidation problems." International journal for numerical and analytical methods in geomechanics **32**(9): 1023-1050.

Oñate, E., M. A. Celigueta, S. R. Idelsohn, F. Salazar and B. Suárez (2011). "Possibilities of the particle finite element method for fluid–soil–structure interaction problems." Computational Mechanics **48**(3): 307.

Oñate, E., S. R. Idelsohn, F. Del Pin and R. Aubry (2004). "The Particle Finite Element Method - An Overview." International Journal of Computational Methods **01**(02): 267-307.

Owen, P., P. W. Cleary and C. Meriaux (2009). "Quasi-static fall of planar granular columns: comparison of 2D and 3D discrete element modelling with laboratory experiments." Geomechanics and Geoengineering: An International Journal **4**(1): 55-77.

Qiu, G., S. Henke and J. Grabe (2011). "Application of a Coupled Eulerian–Lagrangian approach on geomechanical problems involving large deformations." Computers and Geotechnics **38**(1): 30-39.

Rzadkiewicz, S. A., C. Mariotti and P. Heinrich (1997). "Numerical simulation of submarine landslides and their hydraulic effects." Journal of Waterway, Port, Coastal, and Ocean Engineering **123**(4): 149-157.

Sabetamal, H., J. P. Carter, X. Zhang and D. Sheng (2021). "Coupled analysis of full flow penetration problems in soft sensitive clays." Computers and Geotechnics **133**: 104054.

Salazar, F., J. Irazábal, A. Larese and E. Oñate (2016). "Numerical modelling of landslide-generated waves with the particle finite element method (PFEM) and a non-Newtonian flow model." International Journal for Numerical and Analytical Methods in Geomechanics **40**(6): 809-826.

Soga, K., E. Alonso, A. Yerro, K. Kumar and S. Bandara (2016). "Trends in large-deformation analysis of landslide mass movements with particular emphasis on the material point method." Géotechnique **66**(3): 248-273.

Tian, Y., M. J. Cassidy, M. F. Randolph, D. Wang and C. Gaudin (2014). "A simple implementation of RITSS and its application in large deformation analysis." Computers and Geotechnics **56**: 160-167.

Tolooiyan, A. and K. Gavin (2011). "Modelling the Cone Penetration Test in sand using Cavity Expansion and Arbitrary Lagrangian Eulerian Finite Element Methods." Computers and Geotechnics **38**(4): 482-490.

Tran, Q.-A. and W. Sołowski (2019). "Generalized Interpolation Material Point Method modelling of large deformation problems including strain-rate effects – Application to penetration and progressive failure problems." Computers and Geotechnics **106**: 249-265.

Trujillo-Vela, M. G., S. A. Galindo-Torres, X. Zhang, A. M. Ramos-Cañón and J. A. Escobar-Vargas (2020). "Smooth particle hydrodynamics and discrete element method coupling scheme for the simulation of debris flows." Computers and Geotechnics **125**: 103669.

Wang, B., P. J. Vardon and M. A. Hicks (2018). "Rainfall-induced slope collapse with coupled material point method." Engineering Geology **239**: 1-12.

Wang, L., X. Zhang, S. Zhang and S. Tinti (2021). "A generalized Hellinger-Reissner variational principle and its PFEM formulation for dynamic analysis of saturated porous media." Computers and Geotechnics **132**: 103994.

Yang, E., H. H. Bui, H. De Sterck, G. D. Nguyen and A. Bouazza (2020). "A scalable parallel computing SPH framework for predictions of geophysical granular flows." Computers and Geotechnics **121**: 103474.

Yuan, W.-H., K. Liu, W. Zhang, B. Dai and Y. Wang (2020). "Dynamic modeling of large deformation slope failure using smoothed particle finite element method." Landslides **17**(7): 1591-1603.

Yuan, W.-H., B. Wang, W. Zhang, Q. Jiang and X.-T. Feng (2019). "Development of an explicit smoothed particle finite element method for geotechnical applications." Computers and Geotechnics **106**: 42-51.

Yuan, W.-H., W. Zhang, B. Dai and Y. Wang (2019). "Application of the particle finite element method for large deformation consolidation analysis." Engineering Computations **36**(9): 3138-3163.

Zhang, W., W. Yuan and B. Dai (2018). "Smoothed Particle Finite-Element Method for Large-Deformation Problems in Geomechanics." International Journal of Geomechanics **18**(4): 04018010.

Zhang, X., Y. Ding, D. Sheng, S. W. Sloan and W. Huang (2016). "Quasi-static collapse of two-dimensional granular columns: insight from continuum modelling." Granular Matter **18**(3): 41.

Zhang, X., K. Krabbenhoft, D. M. Pedroso, A. V. Lyamin, D. Sheng, M. V. da Silva and D. Wang (2013). "Particle finite element analysis of large deformation and granular flow problems." Computers and Geotechnics **54**: 133-142.

Zhang, X., K. Krabbenhoft and D. Sheng (2014). "Particle finite element analysis of the granular column collapse problem." Granular Matter **16**(4): 609-619.

Zhang, X., K. Krabbenhoft, D. Sheng and W. Li (2014). "Numerical simulation of a flow-like landslide using the particle finite element method." Computational Mechanics **55**(1): 167-177.

Zhang, X., E. Oñate, S. A. G. Torres, J. Bleyer and K. Krabbenhoft (2019). "A unified Lagrangian formulation for solid and fluid dynamics and its possibility for modelling submarine landslides and their consequences." Computer Methods in Applied Mechanics and Engineering **343**: 314-338.

Zhang, X., D. Sheng, G. P. Kouretzis, K. Krabbenhoft and S. W. Sloan (2015). "Numerical investigation of the cylinder movement in granular matter." Phys Rev E Stat Nonlin Soft Matter Phys **91**(2): 022204.

Zhang, X., D. Sheng, S. W. Sloan and K. Krabbenhoft (2016). "Second-order cone programming formulation for consolidation analysis of saturated porous media." Computational Mechanics **58**(1): 29-43.

Zhang, X., L. Wang, K. Krabbenhoft and S. Tinti (2019). "A case study and implication: particle finite element modelling of the 2010 Saint-Jude sensitive clay landslide." Landslides **17**(5): 1117-1127.

Zhou, L., X. Chu, X. Zhang and Y. Xu (2016). "Numerical investigations on breakage behaviour of granular materials under triaxial stresses." Geomechanics and Engineering **11**(5): 639-655.

Zhu, F. and J. Zhao (2021). "Interplays between particle shape and particle breakage in confined continuous crushing of granular media." Powder Technology **378**: 455-467.